Weakly breaking waves in the presence of surfactant micelles

Xinan Liu[*] and James H. Duncan[†]

Department of Mechanical Engineering, University of Maryland, College Park, Maryland 20742, USA

(Received 11 April 2007; revised manuscript received 27 August 2007; published 7 December 2007)

Mechanically generated weakly breaking waves were studied experimentally in clean water and water with a soluble surfactant whose bulk concentration was above the critical micelle concentration (CMC). For the surfactant case, the breaker, which forms a surface-tension-dominated spilling breaker in clean water [wave frequencies 1.42 to 1.15 Hz, see Duncan *et al.*, J. Fluid Mech. **379**, 191 (1999)], ranges from a spiller at the highest frequency to an overturning wave with a plunging microjet at the lowest frequency. It is shown that this behavior is consistent with that of a wave in a pure liquid with a lower surface tension than water rather than water with a surfactant monolayer. The analysis of the geometrical characteristics of the breaking surface generated by the jet impact on the front face of the wave crest indicates a patch of more violent turbulence suggesting an increase of air-sea transfer compared to the clean water case.

[2]Breaking waves dominate the surfaces of oceans and lakes and are central to studies of air-sea transfer processes (heat, mass, momentum, and energy), large- and small-scale ocean current systems, remote sensing, and weather forecasting [1–6]. The study of breaking water waves is also relevant to studies of other physical phenomena including breaking Rossby waves in the stratosphere [7], shoaling internal waves in the ocean [8], shock waves in stellar atmospheres [9] and micron waves breaking at the edge of laser-liquified indium pools [10]. Surfactants (usually organic compounds) are ubiquitous in natural bodies of water and manmade solutions. These surfactants adsorb onto the liquid free surface and thereby lower the ambient surface tension and create surface elasticity and viscosity. These changes in surface dynamic properties can have dramatic effects on a broad class of interfacial flows including capillary waves [11–15], air bubbles, and liquid droplets [16]. When the surfactant bulk concentration reaches a critical value, called the critical micelle concentration (CMC), micelles are formed in the bulk and influence the adsorption/desorption kinetics of surfactants to the surface and thereby the surface dynamic properties, see Ref. [17]. These effects have been studied to a limited extent in low-Reynolds-number flows including liquid jets [18,19], the stability of thin films [20], and two phase mixtures [21]. In this paper, we present an experimental investigation of breaking waves with wavelengths of about 1 m in clean water and in water with a soluble surfactant whose concentration is just above the CMC. The results are applicable to other high-Reynolds-number free surface flows.

The experiments are a continuation of our previous work [11,12,22–26] and were performed in a tank that is 14.8 m long and 1.22 m wide with a water depth of 0.8 m. Weakly breaking waves were generated mechanically from dispersively focused wave packets consisting of the sum of 32 sinusoidal components with frequencies equally spaced around an average f_0. The values of f_0 in this study were 1.15, 1.26, and 1.42 Hz and the nondimensional overall amplitudes (A/λ_0) of the wave-maker motion ranged from 0.0487 to 0.0505, where λ_0 is the wavelength corresponding to f_0 via linear theory, $\lambda_0 = g/2\pi f_0^2$ where g is gravity (see Ref. [22]). The crest profiles of the waves were measured photographically using a laser-induced-fluorescence technique that employs a high-speed movie camera set at 300 frames per second (see Ref. [12]). These measurements were taken from an instrument carriage that moves along the tank with the crest of the breaker.

Using the procedures described in Ref. [12], a set of six surfactant solutions was created in the wave tank. These solutions consist of relatively clean water (data set denoted as CLEAN) and water with five bulk concentrations of the soluble surfactant Triton X-100 (denoted as TX1, lowest concentration, to TX5, highest concentration equal to 6.61 $\times 10^{-5}$ mol/l). As pointed out in Ref. [12], this large tank of water undoubtedly contains other surfactants as well. The dynamic properties of the free surface in the wave tank were measured *in situ* using the equipment and procedures described in Ref. [23]. For all conditions, the ambient surface tension σ_a and the surface pressure isotherms were measured with a Whilhelmy plate combined with an *in situ* Langmuir trough. The value of σ_a is obtained when the Langmuir trough is first lowered onto the water surface. The surface pressure isotherms are measured by monitoring the surface pressure ($\pi = \sigma_c - \sigma$, where σ_c is the surface tension of clean water and σ is the instantaneous surface tension) while compressing the surface area $(\bar{A})$ within the trough over a period of 2 min. The isotherms are plots of π versus $\ln(\bar{A}/\bar{A}_0)$, where $\bar{A}_0$ is the initial value of $\bar{A}$. Plots of σ_a versus bulk concentration for all the surfactant solutions and the surface pressure isotherms for solutions CLEAN, TX1, and TX5 are shown in Figs. 1(a) and 1(b), respectively. (Data for solutions TX1 to TX4 can be found in Ref. [12].) As can be seen in Fig. 1(a), the ambient surface tension decreases with increasing surfactant bulk concentration. In the clean-water surface pressure isotherm, Fig. 1(b), the surface pressure remains at zero until the surface is compressed to about 25% of its original area indicating that there is a very low concentration of surfactant on the free surface under ambient conditions. For solution TX1, the surface pressure is nonzero initially
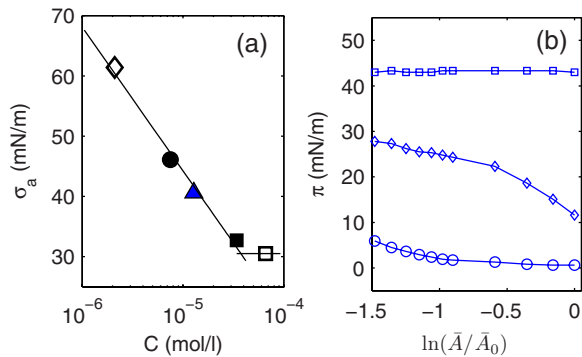
---

*xliu@umd.edu

†duncan@umd.edu

FIG. 1. (Color online) The surface dynamic properties of TX-100 solutions. (a) The ambient surface tension as a function of the bulk concentration (C, in mol/l) of Triton X-100 in the wave tank. The negatively sloped straight line is a least-square fit to the left four data points while the horizontal line is extrapolated from the right data point ($\square$) corresponding to the surfactant solution (TX5), see below. The intersection of these two lines is defined as the critical micelle concentration (CMC). (b) The static pressure isotherms (the surface pressure versus the logarithm of the compression ratio of the surface area). Clean water, $\bigcirc$ (CLEAN) and two Triton X-100 solutions, $\diamond$ (TX1), $C=2.1\times10^{-6}$ and $\square$ (TX5), $C=6.61\times10^{-5}$.

and begins to increase immediately upon surface compression. At the highest surfactant concentration (TX5), the surface pressure remains at the ambient level (30.5 mN/m) throughout the compression. This latter behavior is indicative of reaching or exceeding the CMC. Since above the CMC the ambient surface tension is independent of bulk concentration, a line of surface pressure versus concentration in this region is horizontal. In Fig. 1(a), the intersection of the horizontal line that goes through the TX5 value and the sloped line fitted to data points TX1 to TX4 occurs at 3.5 $\times10^{-5}$ mol/l, defined as the CMC. It should be mentioned that the CMC of Triton X-100 in carefully controlled experiments with purified chemicals and distilled water was found to be 1.55×10^{-4} mol/l [28]. This difference is likely due to impurities in the present experiments [11].

Figure 2 show three sets of three photographs from highspeed movies of spilling breakers in solutions CLEAN, TX1, and TX5, respectively. The wave frequency and nondimensional wave maker amplitude were the same ($f_0=1.42$ Hz and $A/\lambda_0=0.0487$) in all three cases. In these images, the upper edge of the wavy light region is the wave crest profile at the central line of the tank and the wave propagates from the right to left. In all three solutions, the wave behavior is qualitatively similar. The breaking starts with the formation of a bulge on the forward face of the wave and the appearance of capillary waves upstream (to the left) of the leading edge (toe) of the bulge (first images). A little while later, the toe begins to move down the wave face and the capillary waves are compressed (second images). This is followed by the appearance of a train of large ripples generated between the toe and the wave crest (third images). The wave behaviors shown in solutions CLEAN and TX1 are similar to the wave behaviors shown in Ref. [12] in the same solutions but for a wave frequency of 1.15 Hz and $A/\lambda_0=0.0505$. In clean water, the bulge is round and the capillary waves have large amplitude. For a relatively small amount of surfactant (TX1), the bulge flattens out and the capillary waves are diminished. It was shown in Ref. [12] that as the surfactant concentration is increased further, the bulge becomes more round again and the capillary waves diminish further. In solution TX5, the bulge is round and the capillary waves are again visible, though small. Duncan *et al.* [22] noted that for similar breakers in clean water, the size and shape of the bulge and capillary waves are independent of wave frequency and argued that the size of these features therefore scales with $\sqrt{\sigma_a/\rho g}$, where ρ is the water density. A similar result was found in numerical calculations by Longuet-Higgins [27]. Figure 3(a) shows a comparison of the wave crest profiles taken from the left images shown in Figs. 2(a) and 2(c), which were exposed at the instant before the toe began to move down the wave face, in solutions CLEAN (solid curve) and TX5 (dashed-dot curve). Figure 3(b) shows the same profiles scaled by $\sqrt{\sigma_a/\rho g}$. As can be seen from the plots, without scaling, the crest shapes are similar but the features differ in size, while with scaling the two curves match well. This is not true when the breakers in TX1 to TX4 are compared to the CLEAN case (see Ref. [12]).

Figure 4 contains three rows of four images from movies of three breaking waves in solution TX5. The wave maker motions corresponding to the top, middle and bottom rows of images had average frequencies of $f_0=1.42$, 1.26 and
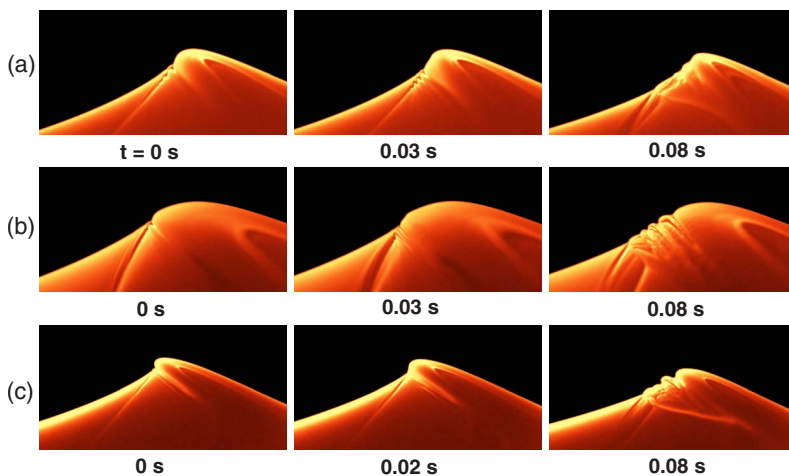

FIG. 2. (Color online) Photographs from high speed movies of breaking waves generated by a wave-maker motion with central frequency $f_0=1.42$ Hz and nondimensional amplitude $A/\lambda_0=0.0487$ in solutions CLEAN (a), TX1 (b), and TX5 (c). The width of these images is 10 cm in the physical plane and the waves propagate from right to left. The online photographs are colorized to enhance the visibility of small scale features. The number underneath each image shows the time relative to the left image. The times of images in each row were chosen to display significant features for comparison between cases rather than to compare wave shapes at the same instant from case to case.
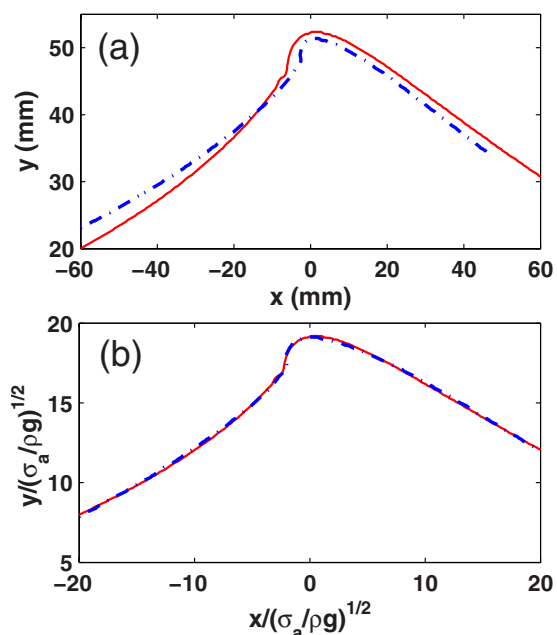
FIG. 3. (Color online) Comparison of the wave crest profiles of breaking waves generated by a wave-maker motion with central frequency $f_0 = 1.42$ Hz and nondimensional amplitude A/λ_0 =0.0487 in solutions CLEAN (solid line) and TX5 (dashed-dot line). (a) Comparison of wave crest profiles at the moment just before the toes start to move [left images in Figs. 2(a) and 2(c)]. (b) Comparison of wave crest profiles shown in (a), but with the horizontal and vertical coordinates scaled by the capillary length scale $\sqrt{\sigma_a/\rho g}$, where σ_a is the ambient surface tension, ρ is the water density, and g is gravity. The dashed-dot curve is shifted vertically after scaling so that both curves are aligned at the wave crest.

1.15 Hz, respectively, and the same nondimensional amplitude ($A/\lambda_0 = 0.0505$). As can be seen from the top row (f_0 =1.42 Hz) of the figure, compared to the breaker shown in Fig. 2(c) ($f_0 = 1.42, A/\lambda_0 = 0.0487$) the bulge points forward, as if forming a plunging jet from the crest. In spite of these initial differences, the subsequent breaking processes in the two cases are qualitatively the same. At the wave frequency 1.26 Hz (Fig. 4, middle row of images) the initial bulge shape is even more jetlike. However, very soon after the jet

tip forms, fluid collapses underneath the jet base (second image). After this, the breaking proceeds in the same spilling manner as mentioned above. For $f_0 = 1.15$ Hz (bottom row of images), the breaking process is initiated by the formation of a microjet on the forward face of the wave crest. The time history of the profile of this breaker is shown in Fig. 5. As can be seen in the third row of images in Fig. 4 and the profiles in Fig. 5, the jet projects forward from the highest point on the wave profile (first image and profile I) and falls down under the influence of gravity (second image and profile II). After a short time, the jet reenters the front face of the wave engulfing a tube of air (third image and profile III). A small splash quickly projects out from the impact site. This is then followed by a much more energetic splash (fourth image and profile IV).

Figure 6(a) shows the wave crest profile of the left image of the bottom row in Fig. 4 along with the trajectory of the jet tip before impact on the wave surface, circles. Plots of the jet tip horizontal and vertical positions versus time are shown in Figs. 6(b) and 6(c), respectively. As can be seen in these plots, the trajectory of the jet tip is parabolic; however, it is interesting to notice that the vertical acceleration of the jet tip is only 0.46g rather than g. It should be kept in mind that the jet tip is a geometrical feature rather than a center of mass. Thus, accelerations other than g are expected. Also, surface tension, air resistance and a nonuniform air pressure distribution surrounding the jet may affect the acceleration [29].

Figure 7 shows three geometrical features (L_b, h_0, and h_1) describing the breaking region on the wave crest profile [as defined in the inset to Fig. 7(a) and the caption of Fig. 7] versus time for the CLEAN and TX5 cases ($f_0 = 1.15$ Hz and $A/\lambda_0 = 0.0505$). The data show that in the TX5 case the breaking zone length (L_b) is longer and the two thicknesses (h_1 and h_0) are much larger. This probably indicates that the free surface turbulence and the local air-water transfer rates of heat and mass in TX5 are higher than in clean water.

Numerical calculations using a potential flow boundary element method [30] have been used by Tulin [31] to explore the effect of surface tension on the initiation of breaking in waves generated by the side-band instability mechanism. The calculations showed that for a fixed surface tension, as the wavelength decreases the breaking process changes from a
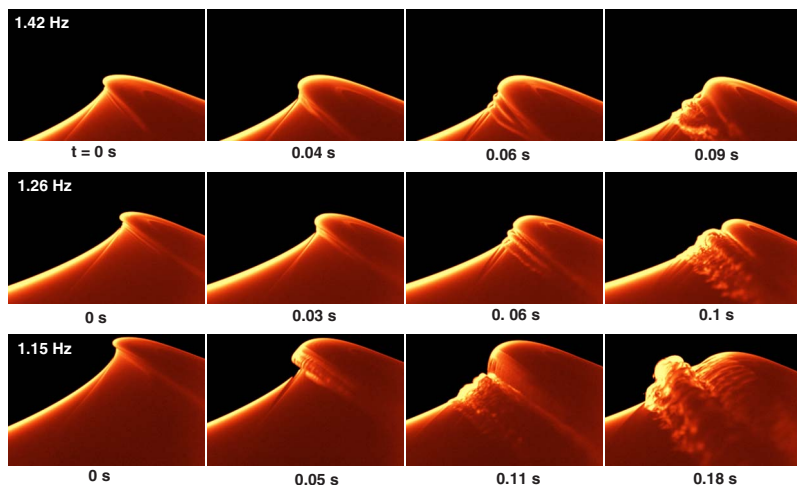

FIG. 4. (Color online) Photographs of breaking waves generated with three wave maker frequencies ($f_0 = 1.42$, 1.26 and 1.15 Hz) and the same nondimensional amplitude ($A/\lambda_0 = 0.0505$) in solution TX5. The width of each image is 10 cm and the number underneath each image shows the time relative to the left image. The times of the images in each row were chosen to display significant features for comparison between cases rather than to compare wave shapes at the same instant from case to case.
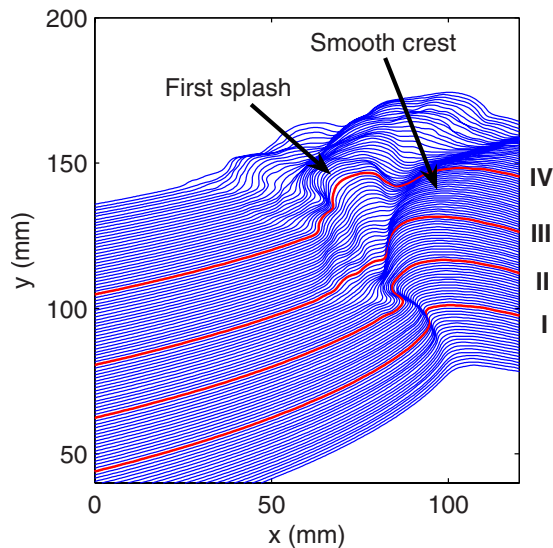
FIG. 5. (Color online) The crest profile history of the breaker with a wave-maker motion of $f_0 = 1.15$ Hz and $A = 0.0505\lambda_0$ in solution TX5. The figure includes 108 profiles measured in 0.36 s. For clarity, each profile is plotted 1 mm above the previous one. The thick lines with Roman numerals correspond to the bottom row of images in Fig. 4 (I=0 s, II=0.05 s, III=0.11 s, and IV=0.18 s).

plunging jet to the bulge-capillary ripple system shown in the top row of images in Fig. 2. This transition occurs between one of their calculations at a Weber number ($We = \rho g \lambda_0^2 / \sigma_a$) of 5.4×10^5 (plunging jet) and another calculation at $We = 3.4 \times 10^4$. Using the ambient surface tension in TX5 and
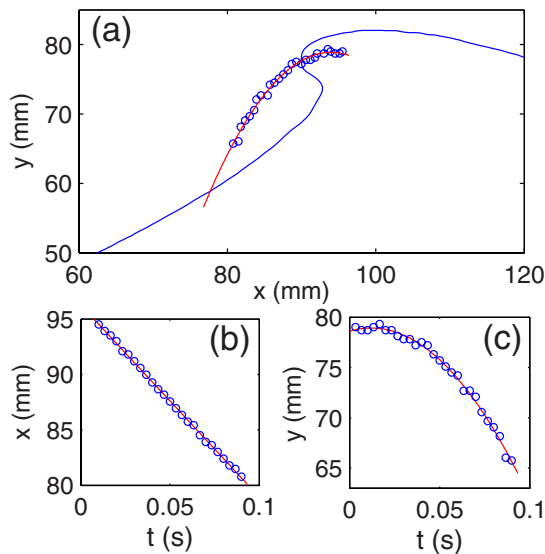

FIG. 6. (Color online) The trajectory of the jet tip of the breaker with a wave-maker motion of $f_0 = 1.15$ Hz and $A = 0.0505\lambda_0$ in the solution TX5. (a) A single wave profile (I from Fig. 5) and the trajectory of the tip of the jet. The solid line is a parabola fitted to the experimental data. (b) and (c) The horizontal and vertical coordinates of the jet tip versus time, respectively. The straight line in (b) and the parabola in (c) are fitted to the experimental data using a least square method. The vertical acceleration obtained from the curve fitting is 4.5 m/s².
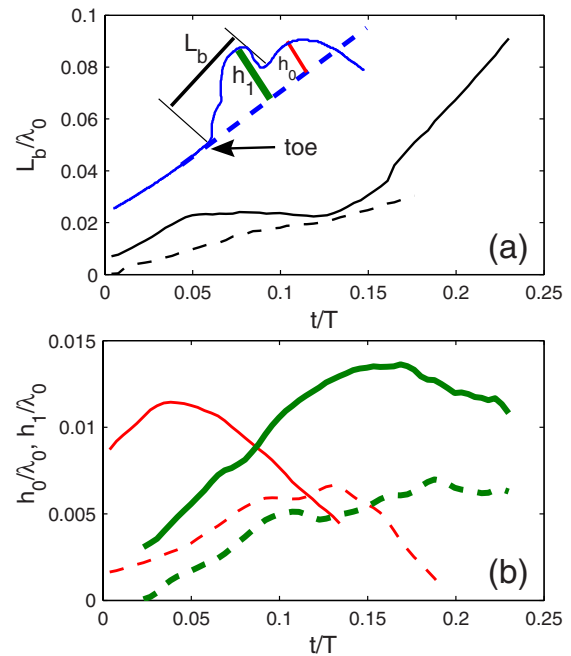

FIG. 7. (Color online) The geometrical properties of the breaker with a wave-maker motion of $f_0 = 1.15$ Hz and $A = 0.0505\lambda_0$. (a) The drawing in the up-left corner defines three geometrical parameters (L_b, h_0, and h_1) describing the breaking region on the wave crest. The solid curve is crest profile IV in Fig. 5 and the straight dashed line is the tangent to the smooth free surface upstream (left) of the toe. The thicknesses h_1 and h_0 are the maximum perpendicular distances from the dashed line to the surface of the first splash and the smooth crest (see Fig. 5), respectively. The length L_b is the distance from the toe to the boundary between the smooth crest and the first splash. The main plot shows L_b versus time after the jet hits the front surface of the wave (TX5, solid line) and after the toe begins its motion (CLEAN, dashed line). (b) The thicknesses h_0 (thin lines) and h_1 (thick lines) versus time in solution TX5 (solid lines) and in solution CLEAN (dashed lines).

$\lambda_0 = g / 2\pi f_0^2$, the transition in the present measurements of weakly breaking waves generated from dispersively focused wave packets with $A/\lambda_0 = 0.0505$ occurs between $We = 4.5 \times 10^5$ (plunging jet) and 1.9×10^5. It is also interesting to note that the shape of the wave crest and plunging jet are quite similar in the calculations and experiments.

The above experimental results and the comparison with potential flow calculations with constant surface tension indicate that in TX5, the wave crest behavior is nearly identical to the behavior of waves in a liquid with low surface tension rather than waves in a surfactant solution. For all other surfactant conditions in our previous work (all at concentrations below the CMC), the wave profiles are not just versions of the clean water case scaled by $\sqrt{\sigma_a / \rho g}$, as they are here. This statement includes the unusually shaped jet, described in Ref. [11] that issued from a point below the wave crest in a solution with a high concentration of sodium dodecyl sulfate (but still below the CMC). The reason for the interesting wave behavior shown herein probably lies in the very high surfactant surface adsorption-desorption rates found at concentrations above the CMC; see Ref. [28] for measurements in pure Triton X-100. Using longitudinal surfactant wave

methods, Noskov *et al.* [32] have shown that due to this high rate of adsorption and desorption (in a different surfactant solution), the surface elasticity and viscosity greatly diminish for concentrations at or above the CMC for low frequency waves. In the present experiments, longitudinal waves were generated and measured at concentrations below the CMC (Ref. [12]), but using the same generation parameters no longitudinal waves were detected in solution TX5, indicating very low values of surface elasticity. Thus, it is likely that with the present gravity wave phenomenon at frequencies of about 1 Hz, the surface has little surface elasticity or viscosity, rendering it dynamically similar to the surface of a liquid with low surface tension rather than a surfactant monolayer. Our results also support the interpretation given by Stebe *et al.* [21] for slug flow behavior in capillary tubes at very low Reynolds numbers (in contrast to the present high Reynolds number case) and surfactant concentrations above the CMC.

[1] M. L. Banner and D. H. Peregrine, Annu. Rev. Fluid Mech. **25**, 373 (1993).

[2] M. L. Banner and X. Tian, Phys. Rev. Lett. **77**, 2953 (1996).

[3] W. K. Melville, Annu. Rev. Fluid Mech. **28**, 279 (1996).

[4] S. A. Thorpe, Nature (London) **318**, 519 (1985).

[5] A. T. Jessup, C. J. Zappa, M. R. Loewen, and V. Hesany, Nature (London) **385**, 52 (1997).

[6] G. L. Mellor and A. F. Blumberg, J. Phys. Oceanogr. **34**, 693 (2004).

[7] M. E. Mcintyre and T. N. Palmer, Nature (London) **305**, 593 (1983).

[8] G. N. Ivey and R. I. Nokes, J. Fluid Mech. **204**, 479 (1989).

[9] G. Wallerstein and S. Elgar, Science **256**, 1531 (1992).

[10] S. Lugomer and N. J. Zabusky, Appl. Phys. Lett. **87**, 204101 (2005).

[11] X. Liu and J. H. Duncan, Nature (London) **421**, 520 (2003).

[12] X. Liu and J. H. Duncan, J. Fluid Mech. **567**, 433 (2006).

[13] E. H. Lucassen-Reynders and J. Lucassen, Adv. Colloid Interface Sci. **2**, 347 (1969).

[14] E. J. Bock and J. A. Mann, Jr., J. Colloid Interface Sci. **129**, 501 (1989).

[15] W. Alpers and H. Huhnerfuss, J. Geophys. Res. **94**, 6251 (1989).

[16] V. G. Levich, *Physicochemical Hydrodynamics* (Prentice-Hall, Englewood Cliffs, 1962).

[17] D. A. Edwards, H. Brenner, and D. T. Wasan, *Interfacial Transport Processes and Rheology* (Butterworth-Heinemamm, Boston, 1991).

[18] D. M. Colegate and C. D. Bain, Phys. Rev. Lett. **95**, 198302 (2005).

[19] M. Weiss, R. C. Darton, T. Battal, and C. D. Bain, Ind. Eng. Chem. Res. **45**, 2235 (2006).

[20] S. S. Patel, K. Kumar, D. O. Shah, and J. J. Delfino, J. Colloid Interface Sci. **183**, 603 (1996).

[21] K. J. Stebe, S. Y. Lin, and C. Maldarelli, Phys. Fluids A **A3**, 3 (1991).

[22] J. H. Duncan, H. Qiao, H. Philomin, and A. Wenz, J. Fluid Mech. **379**, 191 (1999).

[23] X. Liu, J. H. Duncan, G. M. Korenowski, and J. S. Kelly, J. Geophys. Res. **112**, C06005 (2007).

[24] J. H. Duncan, H. Philomin, H. Behres, and J. Kimmel, Phys. Fluids **6**, 2558 (1994).

[25] J. H. Duncan, H. Philomin, H. Qiao, and J. Kimmel, Phys. Fluids **6**, S2 (1994).

[26] H. Qiao and J. H. Duncan, J. Fluid Mech. **379**, 191 (1999).

[27] M. S. Longuet-Higgins, J. Phys. Oceanogr. **96**, 1957 (1996).

[28] A. V. Makievski, V. B. Faierman, and P. Joos, J. Colloid Interface Sci. **166**, 6 (1994).

[29] C. Song and A. I. Sirviente, Phys. Fluids **16**, 2649 (2004).

[30] M. S. Longuet-Higgins and E. D. Cokelet, Proc. R. Soc. London, Ser. A **350**, 1 (1976).

[31] M. P. Tulin, in *Waves and Nonlinear Processes in Hydrodynamics*, edited by J. Grue, B. Gjevik, and J. E. Weber (Kluwer, Dordrecht, 1996), p. 177.

[32] B. A. Noskov, D. A. Alexandrov, and R. Miller, J. Colloid Interface Sci. **219**, 250 (1999).